Statistics of temperature and thermal energy dissipation rate in low-Prandtl number turbulent thermal convection EP

Ao Xu (徐翱) iD, Le Shi (史乐) iD, and Heng-Dong Xi (郗恒东) iD

COLLECTIONS

EP This paper was selected as an Editor's Pick
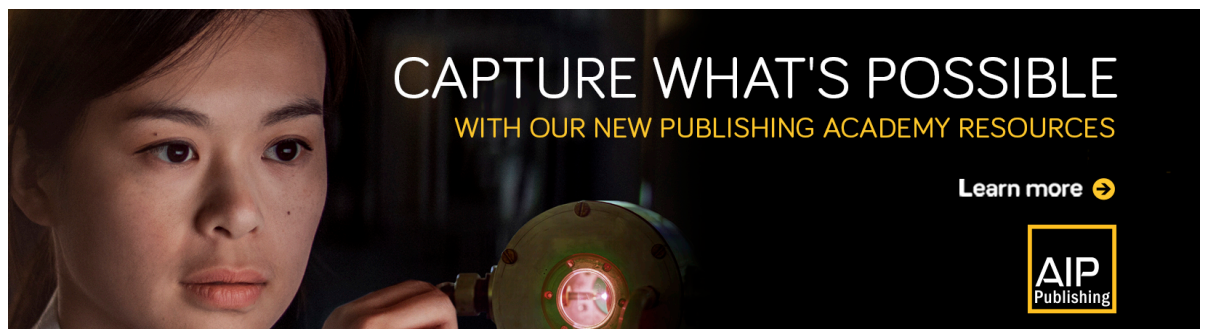
View Online

Export Citation

CrossMark

Statistics of temperature and thermal energy dissipation rate in low-Prandtl number turbulent thermal convection ᴱᴾ

View Online   Export Citation   CrossMark

Ao Xu (徐翱),[1] 🆔 Le Shi (史乐),[2] 🆔 and Heng-Dong Xi (郗恒东),[1,a)] 🆔

AFFILIATIONS

[1] School of Aeronautics, Northwestern Polytechnical University, Xi'an 710072, China
[2] State Key Laboratory of Electrical Insulation and Power Equipment, Center of Nanomaterials for Renewable Energy,
School of Electrical Engineering, Xi'an Jiaotong University, Xi'an 710049, China

a) Electronic mail: hengdongxi@nwpu.edu.cn

ABSTRACT

We report the statistical properties of temperature and thermal energy dissipation rate in low-Prandtl number turbulent Rayleigh-Bénard convection. High resolution two-dimensional direct numerical simulations were carried out for the Rayleigh number (Ra) of $10^6 \leq Ra \leq 10^7$ and the Prandtl number (Pr) of 0.025. Our results show that the global heat transport and momentum scaling in terms of Nusselt number (Nu) and Reynolds number (Re) are $Nu = 0.21Ra^{0.25}$ and $Re = 6.11Ra^{0.50}$, respectively, indicating that scaling exponents are smaller than those for moderate-Prandtl number fluids (such as water or air) in the same convection cell. In the central region of the cell, probability density functions (PDFs) of temperature profiles show stretched exponential peak and the Gaussian tail; in the sidewall region, PDFs of temperature profiles show a multimodal distribution at relatively lower Ra, while they approach the Gaussian profile at relatively higher Ra. We split the energy dissipation rate into contributions from bulk and boundary layers and found the *locally averaged* thermal energy dissipation rate from the boundary layer region is an order of magnitude larger than that from the bulk region. Even if the much smaller volume occupied by the boundary layer region is considered, the *globally averaged* thermal energy dissipation rate from the boundary layer region is still larger than that from the bulk region. We further numerically determined the scaling exponents of globally averaged thermal energy dissipation rates as functions of Ra and Re.

Published under license by AIP Publishing. https://doi.org/10.1063/1.5129818

I. INTRODUCTION

Thermal convection occurs ubiquitously in nature and has wide applications in industry. When the kinematic viscosity of the fluid is much smaller than its thermal diffusivity, the thermal convective flow is called low-Prandtl number convection. Low-Prandtl number convection has found its unique applications in the outer envelope of the Sun,[1] the liquid metal core of the Earth and other planets,[2] the fission reactors of nuclear engineering,[3] the electrodes of liquid metal batteries,[4] and so on. A paradigm for the study of thermal convection is the Rayleigh-Bénard convection, which is a fluid layer heated from the bottom and cooled from the top.[5–9] Challenges on laboratory experiments of low-Prandtl number convection mainly arise from opaque nature of the working fluid, which is usually liquid metal, excluding optical imaging techniques such

as particle image velocimetry or Lagrangian particle tracking. As for direct numerical simulations (DNS), extensive computational resources are needed to resolve the very thin viscous boundary layer in low-Prandtl number convection, where the production of vorticity and shear are strongly enhanced. Due to the above reasons, previous studies on convection in low-Prandtl number fluids (such as liquid mercury and liquid gallium) are relatively fewer compared with that in moderate-Prandtl number fluids (such as water and air). Recent research progress on low-Prandtl number convection includes Vogt *et al.*'s[10] discovery that large-scale circulation takes the form of a jump rope vortex in cells of aspect ratio higher than unity when using liquid gallium as the working fluid. Schumacher *et al.*[11] found that the generation of small-scale vorticity in bulk convection follows the same mechanisms as idealized isotropic turbulence for low-Prandtl number convection. Scheel and Schumacher[2]

identified a transition between the rotationally constrained and the weakly rotating turbulent states in rotating Rayleigh-Bénard convection with liquid gallium that differs substantially from moderate-Prandtl number convection. The main differences are due to more diffuse temperature field, more vigorous velocity field, and coarser yet fewer production of thermal plumes in low-Prandtl number convection.[11–13]

In thermal convection, the global heat transport of the system is measured by the Nusselt number (Nu), which is defined as $Nu = Q/(\chi\Delta_T/H)$. Here, Q is the heat current density across the fluid layer of height H, χ is the thermal conductivity of the fluid, and Δ_T is the imposed temperature difference. The control parameters of the system include the Rayleigh number (Ra), which describes the strength of buoyancy force relative to thermal and viscous dissipative effects via $Ra = \beta g\Delta_T H^3/(\nu\kappa)$, and the Prandtl number (Pr), which describes the thermophysical fluid properties via $Pr = \nu/\kappa$. Here, β, κ, and ν are the thermal expansion coefficient, thermal diffusivity, and kinematic viscosity of the fluid, respectively. g is the gravitational acceleration. In turbulent thermal convection, the energy supplied at large scales cascades to intermediate scales and then to dissipative scales. To quantify the dissipation of kinetic and thermal energies due to fluid viscosity and thermal diffusivity, the kinetic and thermal energy dissipation rates are defined as $\varepsilon_u(\mathbf{x},t) = (\nu/2)\sum_{ij}[\partial_i u_j(\mathbf{x},t) + \partial_j u_i(\mathbf{x},t)]^2$ and $\varepsilon_T(\mathbf{x},t) = \kappa\sum_i[\partial_i T(\mathbf{x},t)]^2$, respectively. Shraiman and Siggia[14] averaged the equations of motion and derived exact relations of global averages of $\varepsilon_u = \langle\varepsilon_u(\mathbf{x},t)\rangle_V$ and $\varepsilon_T = \langle\varepsilon_T(\mathbf{x},t)\rangle_V$. The rigorous global exact relations of $\varepsilon_u = \nu^3 L^{-4}(Nu - 1)RaPr^{-2}$ and $\varepsilon_T = \kappa\Delta_T^2 L^{-2}Nu$ further form the backbone of the Grossman-Lohse (GL) theory on turbulent heat transfer.[15,16] In the GL theory, the energy dissipation rate was split into contributions from bulk and boundary layers, such that the scaling of Nu and Re in the Ra-Pr phase diagram was obtained. Later, Grossmann and Lohse[17] extended the GL theory and considered the role of thermal plumes. They split ε_T into contributions from turbulent background and plumes. Although these two approaches to split energy dissipation involve different physical pictures about the local dynamics of turbulent convection, there is no change in the quantitative functional forms of Nu and Re with Ra and Pr. Based on the analysis of direct numerical simulation data, Emran and Schumacher[18] found, for $Pr = 0.7$ fluid, the probability density functions (PDFs) of ε_T in a cylindrical cell deviate from a log-normal distribution, but fit well by a stretched exponential distribution similar to passive scalar dissipation rate in homogeneous isotropic turbulence.[19] Kaczorowski and Wagner[20] analyzed the contributions of bulk and boundary layers and plumes to the PDFs of the thermal dissipation rate in a rectangular cell of $Pr = 0.7$ fluid. They found the core region scaling changes from pure exponential to a stretched exponential scaling with the increasing of Ra. Zhang et al.[21] investigated statistical properties of ε_u and ε_T in a two-dimensional square cell with $Pr = 0.7$ and $Pr = 5.3$ fluids. They found the ensemble average of the scale of both dissipation rates as $Ra^{-0.18 \text{ to } -0.20}$, in agreement with the prediction of global exact relations.[14] The boundary layer and plume contributions scale as GL theory predictions, while the bulk and background contributions deviate from the GL theory predictions. Within the viscous and thermal boundary layers, the PDFs of kinetic and thermal energy dissipation rates are non-log-normal and

obey approximately a Bramwell-Holdsworth-Pinton distribution.[22] Bhattacharya et al.[23] derived scaling relations for the viscous dissipation rate and viscous dissipation, and their results indicate that although the viscous dissipation rate in the boundary layers is more intense, the viscous dissipation in the bulk is larger than that in the boundary layers, which is caused by the large volume of the bulk region.

In this work, we quantify the statistics of the temperature and the thermal energy dissipation rate in low-Prandtl number Rayleigh-Bénard convection, to further enrich our understandings of the flow dynamics and energy cascade in low-Prandtl number turbulent convection. Here, we choose the working fluid with $Pr = 0.025$ as an example, which corresponds to the typical Prandtl number of liquid gallium or mercury. In contrast to conventional direct numerical simulation (DNS) based on solving the discretized nonlinear Navier-Stokes equations, we adopt the lattice Boltzmann (LB) method as an alternative numerical tool for DNS mainly due to two reasons. One is that the LB method is easy to be implemented and parallelized, benefiting from its local nonlinearity, while the other is that the LB method has lower numerical dissipation compared to conventional second-order computational fluid dynamics methods.[24–26] During the past several decades, the LB method has been successfully applied to DNS of turbulent flows, including decaying homogeneous isotropic turbulence,[27,28] turbulent channel and pipe flows,[29,30] and turbulent thermal convective flows.[31] The rest of this paper is organized as follows: In Sec. II, we first present the mathematical model for the incompressible thermal flow under the Boussinesq approximation, followed by the LB method to obtain velocity and temperature fields. In Sec. III, we first introduce global features in low-Prandtl number thermal convection and then analyze the statistics of temperature and thermal energy dissipation rate. In Sec. IV, main conclusions of the present work are summarized.

II. NUMERICAL METHOD

A. Mathematical model for incompressible thermal flow

We consider incompressible thermal flows under the Boussinesq approximation. The temperature is treated as an active scalar and its influence on the velocity field is realized through the buoyancy term. The viscous heat dissipation and compression work are neglected, and all the transport coefficients are assumed to be constants. The governing equations can be written as

$$\nabla \cdot \mathbf{u} = 0, \tag{1a}$$

$$\frac{\partial \mathbf{u}}{\partial t} + \mathbf{u} \cdot \nabla \mathbf{u} = -\frac{1}{\rho_0}\nabla p + \nu\nabla^2\mathbf{u} + g\beta(T - T_0)\hat{\mathbf{y}}, \tag{1b}$$

$$\frac{\partial T}{\partial t} + \mathbf{u} \cdot \nabla T = \kappa\nabla^2 T, \tag{1c}$$

where $\mathbf{u} = (u, v)$ is the fluid velocity. p and T are the pressure and temperature of the fluid, respectively. ρ_0 and T_0 are the reference density and temperature, respectively. $\hat{\mathbf{x}}$ and $\hat{\mathbf{y}}$ are the unit vectors in the horizontal and vertical directions, respectively. With the scaling

$$\mathbf{x}/H \to \mathbf{x}^*, \quad t/\sqrt{H/(g\beta\Delta_T)} \to t^*, \quad \mathbf{u}/\sqrt{g\beta H\Delta_T} \to \mathbf{u}^*,$$
$$p/(\rho_0 g\beta\Delta_T H) \to p^*, \quad (T - T_0)/\Delta_T \to T^* \tag{2}$$

then Eq. (1a) can be rewritten in the dimensionless form as

$$\nabla \cdot \mathbf{u}^* = 0, \tag{3a}$$

$$\frac{\partial \mathbf{u}^*}{\partial t} + \mathbf{u}^* \cdot \nabla \mathbf{u}^* = -\nabla p^* + \sqrt{\frac{Pr}{Ra}} \nabla^2 \mathbf{u}^* + T^* \tilde{\mathbf{y}}, \tag{3b}$$

$$\frac{\partial T^*}{\partial t} + \mathbf{u}^* \cdot \nabla T^* = \sqrt{\frac{1}{PrRa}} \nabla^2 T. \tag{3c}$$

B. LB model for fluid flows and heat transfer

The LB model to solve fluid flows and heat transfer is based on the double distribution function approach, which consists of a D2Q9 model for the Navier-Stokes equations [i.e., Eqs. (1a) and (1b)] to simulate fluid flows and a D2Q5 model for the convection-diffusion equations [i.e., Eq. (1c)] to simulate heat transfer. In the LB method, to solve Eqs. (1a) and (1b), the evolution equation of the density distribution function is written as

$$f_i(\mathbf{x}+\mathbf{e}_i\delta_t, t+\delta_t) - f_i(\mathbf{x}, t) = -(\mathbf{M}^{-1}\mathbf{S})_{ij}\left[\mathbf{m}_j(\mathbf{x}, t) - \mathbf{m}_j^{(eq)}(\mathbf{x}, t)\right] + \delta_t F_i', \tag{4}$$

where f_i is the density distribution function. $\mathbf{x}$ is the fluid parcel position, t is the time, and δ_t is the time step. $\mathbf{e}_i$ is the discrete velocity along the ith direction. $\mathbf{M}$ is a 9×9 orthogonal transformation matrix that projects the density distribution function f_i and its equilibrium $f_i^{(eq)}$ from the velocity space onto the moment space, such that $\mathbf{m} = \mathbf{M}\mathbf{f}$ and $\mathbf{m}^{(eq)} = \mathbf{M}\mathbf{f}^{(eq)}$. $\mathbf{S} = \text{diag}(s_\rho, s_e, s_\varepsilon, s_j, s_q, s_j, s_q, s_v, s_v)$ is the diagonal relaxation matrix, where the relaxation parameters are chosen as $s_\rho = s_j = 0$, $s_e = s_\varepsilon = s_v = 1/\tau_f$, $s_q = 8(2\tau_f - 1)(8\tau_f - 1)$. Here, τ_f is related with the kinematic viscosity of the fluid via $v = c_s^2(\tau_f - 0.5)$. The forcing term F_i' in the right-hand side of Eq. (4) is given by $\mathbf{F}' = \mathbf{M}^{-1}(\mathbf{I} - \mathbf{S}/2)\mathbf{M}\tilde{\mathbf{F}}$, and the term $\mathbf{M}\tilde{\mathbf{F}}$ is[32]

$$\mathbf{M}\tilde{\mathbf{F}} = [0, 6\mathbf{u} \cdot \mathbf{F}, -6\mathbf{u} \cdot \mathbf{F}, F_x, -F_x, F_y,$$
$$-F_y, 2uF_x - 2vF_y, uF_x + vF_y]^T, \tag{5}$$

where $\mathbf{F} = \rho g\beta(T - T_0)\hat{\mathbf{y}}$. The macroscopic density ρ and velocity $\mathbf{u}$ are obtained from $\rho = \sum_{i=0}^{8} f_i$, $\mathbf{u} = \frac{1}{\rho}\left(\sum_{i=0}^{8} \mathbf{e}_i f_i + \mathbf{F}/2\right)$. To solve Eq. (1c), the evolution equation of the temperature distribution function is written as

$$g_i(\mathbf{x} + \mathbf{e}_i\delta_t, t + \delta_t) - g_i(\mathbf{x}, t) = -(\mathbf{N}^{-1}\mathbf{Q})_{ij}\left[\mathbf{n}_j(\mathbf{x}, t) - \mathbf{n}_j^{(eq)}(\mathbf{x}, t)\right], \tag{6}$$

where g_i is the temperature distribution function. $\mathbf{N}$ is a 5×5 orthogonal transformation matrix that projects the temperature distribution function g_i and its equilibrium $g_i^{(eq)}$ from the velocity space onto the moment space, such that $\mathbf{n} = \mathbf{N}\mathbf{g}$ and $\mathbf{n}^{(eq)} = \mathbf{N}\mathbf{g}^{(eq)}$. $\mathbf{Q} = \text{diag}(0, q_\kappa, q_\kappa, q_e, q_v)$ is the diagonal relaxation matrix. To achieve the isotropy of the fourth-order error term,[33] the relationship for relaxation parameters in the D2Q5 model leads to $q_\kappa = 3 - \sqrt{3}$, $q_e = q_v = 4\sqrt{3} - 6$ and $a_T = 20\sqrt{3}\kappa - 6$, where a_T is a constant in the equilibrium distribution function $\mathbf{n}^{(eq)}$. The macroscopic temperature T is obtained from $T = \sum_{i=0}^{4} g_i$. More numerical details on the lattice Boltzmann method can be found in Refs. 31 and 34–36.

C. Simulation settings

The top and bottom walls of the convection cell are kept at constant cold and hot temperatures, respectively; while the other two vertical walls are adiabatic. All four walls impose no-slip velocity boundary condition. The dimension of the cell is $L \times H$, and we set $L = H$ in this work. Simulation results are provided for the Rayleigh number of $10^6 \leq Ra \leq 10^7$ and the Prandtl number of $Pr = 0.025$. To make sure that the statistically stationary state has been reached and the initial transient effects are washed out, the simulation protocol is as follows: we first check whether the statistically stationary state has reached in every $100t_f$; after that, we check whether the statistically convergent state has reached in every $100t_f$. The average time t_{avg} to obtain statistically convergent results are given in Table I. Here, t_f denotes the free-fall time unit $t_f = \sqrt{H/(g\beta\Delta_T)}$. We also check whether the grid spacing Δ_g and time interval Δ_t are properly resolved by comparing with the Kolmogorov and Batchelor scales. The Kolmogorov length scale is estimated by the global criterion $\eta = HPr^{1/2}/[Ra(Nu - 1)]^{1/4}$, the Batchelor length scale is estimated by $\eta_B = \eta Pr^{-1/2}$, and the Kolmogorov time scale is estimated as $\tau_\eta = \sqrt{v/\langle\varepsilon_u\rangle} = \sqrt{Pr/(Nu - 1)}$. The global heat transport is measured as the volume averaged Nusselt number as $Nu_{vol} = 1 + \sqrt{PrRa}\langle vT\rangle_{V,t}$. From Table I, we can see that grid spacing satisfy $\max(\Delta_g/\eta, \Delta_g/\eta_B) \leq 0.45$, which ensures the spatial resolution. In addition, the time intervals are $\Delta_t \leq 0.000\,55\tau_\eta$, thus guaranteeing an adequate temporal resolution.

In Rayleigh-Bénard convection, in addition to the volume averaged Nusselt number, we can define the average Nusselt number over top and bottom walls as $Nu_{wall} = -1/2(\langle\partial_z T\rangle_{top, t} + \langle\partial_z T\rangle_{bottom, t})$ and the thermal energy dissipation rate based Nusselt number as $Nu_{th} = \sqrt{RaPr}\langle\varepsilon_T\rangle_{V,t}$. If the direct numerical simulation of RB convection is well resolved and statically convergent, the above three definitions of Nusselt numbers should give the same result. Here, the volume averaged Nusselt number Nu_{vol} is chosen as the reference value to calculate its relative differences with other Nusselt numbers, and the differences (denoted by "diff.") are included in brackets in the corresponding columns. From Table II, we can see the differences are around 1%, indicating that Nusselt numbers show good consistency with each other. In addition, to measure the global strength of the convection, the Reynolds number based on root-mean-square (rms) velocity is defined as $Re = \sqrt{\langle u^2 + v^2\rangle_{V,t}}H/v$. Even for convective turbulence at the moderate Rayleigh number of

TABLE I. Spatial and temporal resolutions of the simulations.

Ra	Pr	Mesh size	Δ_g/η	Δ_g/η_B	Δ_t/τ_η	t_{avg}/t_f
1.0×10^6	0.025	769^2	0.39	0.062	5.45×10^{-4}	700
1.3×10^6	0.025	851^2	0.39	0.062	5.22×10^{-4}	2300
1.6×10^6	0.025	901^2	0.40	0.063	5.11×10^{-4}	1400
2.0×10^6	0.025	1001^2	0.38	0.060	4.73×10^{-4}	1000
3.0×10^6	0.025	1025^2	0.43	0.067	4.89×10^{-4}	1400
4.0×10^6	0.025	1101^2	0.43	0.068	4.71×10^{-4}	1000
6.0×10^6	0.025	1201^2	0.45	0.071	4.54×10^{-4}	1300
1.0×10^7	0.025	1537^2	0.42	0.066	3.83×10^{-4}	1000

TABLE II. Nusselt and Reynolds numbers as a function of Rayleigh number.

Ra	Pr	Nu_{vol}	Nu_{wall} (diff.)	Nu_{th} (diff.)	Re
1.0×10^6	0.025	6.28	6.25 (0.38%)	6.35 (1.12%)	6 025.06
1.3×10^6	0.025	6.92	6.97 (0.79%)	7.01 (1.27%)	7 064.86
1.6×10^6	0.025	7.37	7.36 (0.12%)	7.32 (0.59%)	7 789.17
2.0×10^6	0.025	7.72	7.74 (0.28%)	7.73 (0.12%)	8 779.49
3.0×10^6	0.025	8.54	8.57 (0.37%)	8.57 (0.43%)	10 628.02
4.0×10^6	0.025	9.08	9.13 (0.60%)	9.14 (0.74%)	12 208.34
6.0×10^6	0.025	9.93	9.99 (0.60%)	10.00 (0.70%)	14 843.71
1.0×10^7	0.025	11.38	11.39 (0.11%)	11.42 (0.36%)	19 512.48

$Ra = 10^7$, the corresponding Reynolds number of the turbulent flow can reach $Re \sim O(10^4)$.

III. RESULTS AND DISCUSSION

A. Global features

A typical snapshot of an instantaneous flow field and the corresponding temperature, vorticity, and logarithmic thermal energy dissipation rate fields are shown in Fig. 1, and a corresponding video can be viewed in the supplementary material. At the same Ra, low-Prandtl number turbulent thermal convection is more vigorous due to inertial effects. The temperature field is diffusive with the coarse plumes near the top and bottom boundary layers, rather than the filamented plumes in moderate-Prandtl number turbulent thermal convection. The production of vorticity is strong near all the four walls, while intense dissipations of thermal energy occur in regions of detached hot or cold plumes from bottom and top boundary layers, in consistent with previous studies[18,21,37,38] that rising and falling thermal plumes are associated with large amplitudes of thermal energy dissipation rates.

Time-averaged temperature fields and streamlines obtained at $Ra = 10^7$ for both low- and moderate- Prandtl number convection are shown in Figs. 2(a) and 2(b), respectively. Numerical details on DNS of moderate-Prandtl number convection can be found in the Appendix. From Figs. 2(a) and 2(b), we can observe a typical flow pattern of Rayleigh-Bénard convection, where there exists a well-defined LSC, together with counter-rotating corner rolls. Meanwhile, we notice distinguishable differences on the flow pattern in this time-averaged flow field. At a low Prandtl number (i.e., $Pr = 0.025$), the LSC is in the form of a circle, and there exist four secondary corner vortices; at moderate Prandtl number (i.e., $Pr = 5.3$), the LSC is in the form of a tilted ellipse, sitting along a diagonal of the flow cell with two secondary corner vortices that exist along the other diagonal. A similar pattern was reported in a quasi-two-dimensional RB cell at a moderate Prandtl number.[39] We further calculate the probability density functions (PDFs) of the velocity vector orientation θ and plot its time evolution in Figs. 2(c) and 2(d). Each vertical slice is a PDF of θ for an instantaneous velocity field. Here, we count velocity of fluid nodes that belong to the inscribed circle region of the square convection cell. Figure 2(c) indicates the velocity vector orientations have high probability values around 0° (or 360°), 90°, 180°, and 270°, implying the velocities of rising and falling thermal plumes, as well as horizontal "wind." Comparing with Figs. 2(c) and 2(d), we can find the velocity
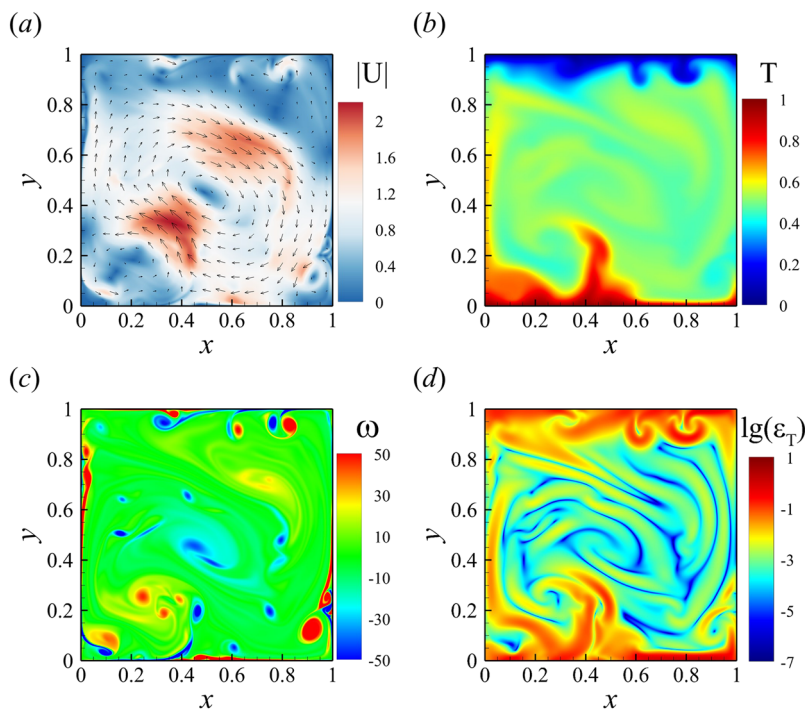

FIG. 1. A typical snapshot of an instantaneous flow field (a) and its corresponding temperature field (b), vorticity field (c), and logarithmic thermal energy dissipation rate field (d) for $Ra = 10^7$ and $Pr = 0.025$.
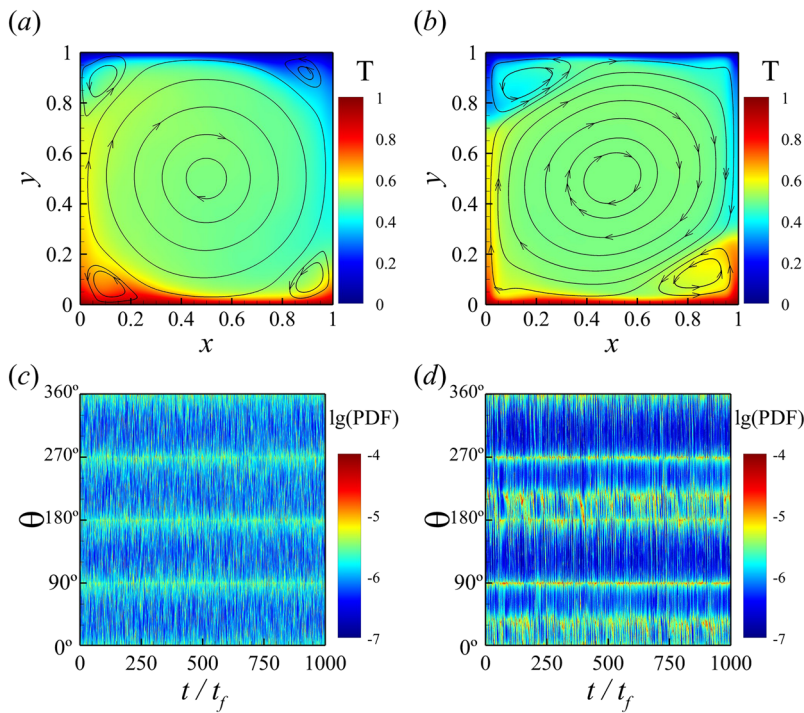
FIG. 2. [(a) and (b)] Time-averaged temperature fields and streamlines, [(c) and (d)] time evolution (from left to right) of the probability density functions (PDFs) of the instantaneous velocity vector orientation θ for $Pr = 0.025$ [(a) and (c)] and $Pr = 5.3$ [(b) and (d)] at $Ra = 10^7$.

vector orientations have additional high probability values around $30°$ and $210°$, suggesting the diagonal orientation of the main roll for $Pr = 5.3$.

The measured Nusselt and Reynolds numbers as functions of Rayleigh number are shown in Figs. 3(a) and 3(b), respectively. The data can be well described by a power-law relation $Nu = 0.21Ra^{0.25}$ and $Re = 6.11Ra^{0.50}$, indicated by the solid lines in the figures. The heat transfer scaling exponent is in general consistent with previous experimental results and direct numerical simulation results obtained in a cylindrical RB cell filled with liquid mercury or liquid gallium,[2,12,40,41] where $Nu \propto Ra^{0.25-0.27}$, while the momentum scaling exponent from the present two-dimensional simulation is larger than that in previous three-dimensional simulations,[12,41] where $Re \propto Ra^{0.44-0.45}$. The above findings indicate that the $Nu(Ra)$ scaling exponent for two- and three-dimensional convection is very

close, while the $Re(Ra)$ scaling exponent is larger in two-dimensional convection. This trend is similar with previous comparison between two- and three-dimensional convection at a moderate Prandtl number.[42] The scaling exponents of $Nu(Ra)$ and $Re(Ra)$ for our low Pr case are lower than those obtained in moderate Pr cases, such as $Pr = 0.7$ case,[21,43] $Pr = 1.0$ case,[44,45] $Pr = 4.4$ case,[46] and $Pr = 5.3$ case,[21] where $Nu \propto Ra^{0.285-0.30}$ and $Re \propto Ra^{0.59-0.62}$, while the prefactors of $Nu(Ra)$ and $Re(Ra)$ for the low Pr case are larger than those obtained in the moderate Pr case.[47]

B. Statistics of temperature

We show the probability density functions (PDFs) of the normalized temperature $(T - \mu_T)/\sigma_T$ measured at the mid-height (i.e., $y = 0.5H$) in two regions: one is in the central region, i.e.,
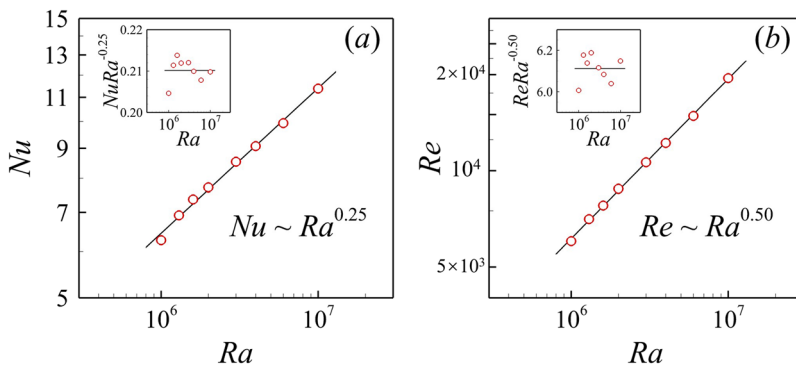

FIG. 3. (a) Nusselt number and (b) Reynolds number as functions of Rayleigh number for $Pr = 0.025$. The solid lines are the power-law fits to the data. The insets are the compensated plots of the data shown in (a) and (b), respectively.
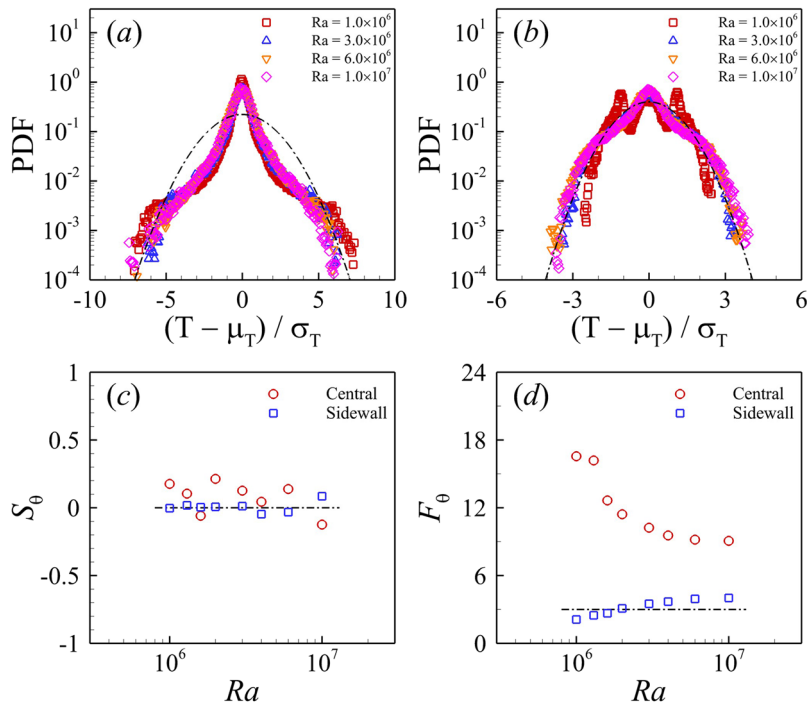
FIG. 4. (a) Probability density functions (PDFs) of the normalized temperature $(T - \mu_T)/\sigma_T$ measured along the line in the central region at mid-height, i.e., $0.25L \leq x \leq 0.75L$ and $y = 0.5H$; the dotted-dashed line represents a Gaussian distribution; (b) PDFs of the normalized temperature measured along the line in the sidewall region at mid-height, i.e., $0 \leq x \leq 0.25L$, $0.75L \leq x \leq L$, and $y = 0.5H$; (c) skewness of the temperature along the same line as that in (a) and (b); the dotted-dashed line represents the value of zero; (d) flatness of the temperature along the same line as that in (a) and (b); the dotted-dashed line represents flatness for a Gaussian distribution.

$0.25L \leq x \leq 0.75L$ [see Fig. 4(a)]; the other is in the sidewall region, i.e., $0 \leq x \leq 0.25L$ and $0.75L \leq x \leq L$ [see Fig. 4(b)]. Here, μ_T and σ_T represent the mean value and standard deviation of T. Generally, the temperature PDFs are symmetric at the mid-height of the convection cell, in agreement with previous findings at moderate-Prandtl number convection.[18,37] To quantitatively describe the asymmetry of the PDFs of the temperature, we calculate the skewness of temperature S_θ as

$$S_\theta(y = 0.5H) = \frac{\langle \theta^3 \rangle_{\mathbf{x},t}}{\langle \theta^2 \rangle_{\mathbf{x},t}^{3/2}}, \qquad (7)$$

where $\theta = T - \mu_T$. The average $\langle \cdot \rangle_{\mathbf{x},t}$ is calculated over time t and along the horizontal line $\mathbf{x}$ in the central or sidewall region. From Fig. 4(c), we can see that the skewness values are around zero in both central and sidewall regions, indicating the rising hot plumes are comparable with the falling cold plumes at the cell mid-height. As for the shapes of the temperature PDF profiles in the central region, the peaks show stretched exponential behavior and the tails show Gaussian behavior for all the considered Rayleigh numbers [indicated by the black dotted-dashed line; see Fig. 4(a)]. In the sidewall region, the temperature PDF profiles show a multimodal distribution at a relatively lower Rayleigh number (e.g., $Ra = 10^6$), indicating the flow state is in the regime transition to hard turbulence;[48,49] at a relatively higher Rayleigh number, the temperature PDF profiles approach the Gaussian profile indicated by the black dotted-dashed line [see Fig. 4(b)]. To quantitatively describe the magnitude of the deviation from Gaussianity, we calculate the flatness of temperature F_θ as

$$F_\theta(y = 0.5H) = \frac{\langle \theta^4 \rangle_{\mathbf{x},t}}{\langle \theta^2 \rangle_{\mathbf{x},t}^2}. \qquad (8)$$

We can see from Fig. 4(d) that the flatness in central and sidewall regions show different trends with the increasing of Rayleigh number. The large differences in these two regions are mainly due to the disparity in the number of plumes, since the central region has relatively few plumes and the sidewall region is dominated by thermal plumes.[50]

C. Statistics of thermal energy dissipation rate

Figure 5(a) shows the PDFs of thermal energy dissipation rates $\varepsilon_T(\mathbf{x}, t)$ obtained over the whole cell and over time, further normalized by their root-mean-square (rms) values. The PDF tails become more extended with the increasing of Ra, implying an increasing degree of small-scale intermittency of the thermal energy dissipation field. We further check whether the thermal energy dissipation fields have a log-normal distribution as proposed by Kolmogorov.[51] Figure 5(b) shows the PDFs of the normalized logarithmic thermal energy dissipation rate $(\log \varepsilon_T - \mu_{\log \varepsilon_T})/\sigma_{\log \varepsilon_T}$, and we can observe clear departures from log-normality for the thermal energy dissipation field, which is mainly due to the intermittent nature of local dissipation. Similar observations have also been made for moderate-Prandtl number convection.[18,21,52]

The time-averaged logarithmic thermal energy dissipation field $\langle \log \varepsilon_T(\mathbf{x}, t) \rangle$ obtained at $Ra = 10^7$ and $Pr = 0.025$ is shown in Fig. 6(a). From the time averaged field, it is seen that the contribution of thermal plumes to thermal energy dissipation is filtered out, and we can only see intense thermal energy dissipation occurs near the top and bottom walls where there are strong temperature gradients. At the sidewall, the thermal energy dissipation rates do not increase significantly due to the adiabatic sidewall boundary conditions. The vertical profiles of $\langle \varepsilon_T(\mathbf{x}, t) \rangle_{x,t}(y)$ that averaged over the horizontal
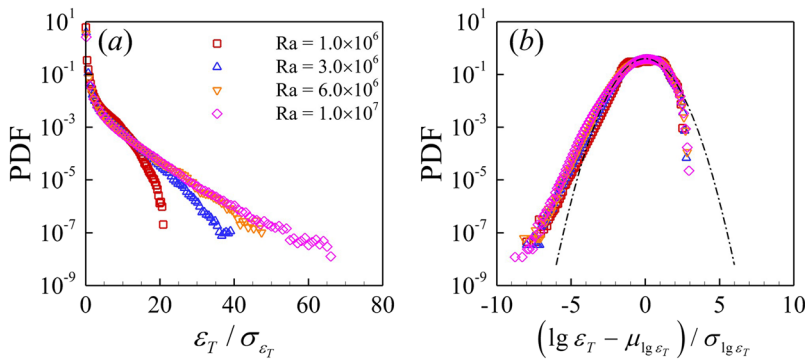
FIG. 5. (a) Probability density functions (PDFs) of the thermal energy dissipation rate $\varepsilon_T(\mathbf{x}, t)$, and (b) PDFs of the normalized logarithmic thermal energy dissipation rate $\log \varepsilon_T(\mathbf{x}, t)$ obtained over the whole cell; the dotted-dashed line represents a log-normal distribution.
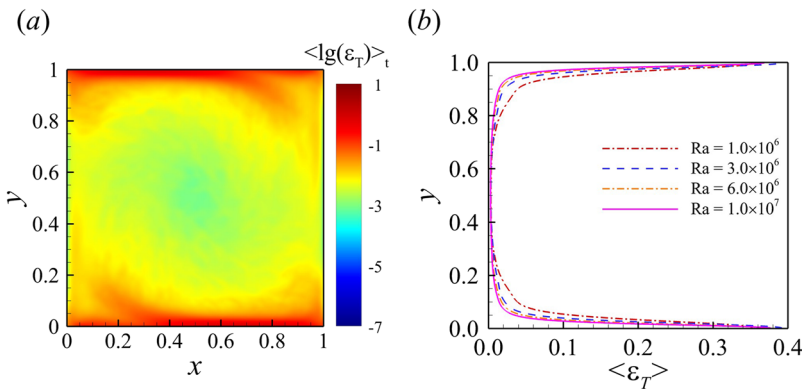

FIG. 6. (a) Time-averaged logarithmic thermal energy dissipation field obtained at $Ra = 10^7$ and $Pr = 0.025$, and (b) vertical profiles of horizontal- and time-averaged thermal energy dissipation rates for $Pr = 0.025$ and various Ra.

direction and over time are shown in Fig. 6(b), which further illustrates the spatial distribution of the thermal energy dissipation rate. The thermal energy dissipation rate remains nearly zero in the bulk and increases rapidly near the top and bottom boundary layers, suggesting intense thermal energy dissipation within thermal boundary layers.

To quantitatively describe the spatial distribution of thermal energy dissipation, the thermal energy dissipation rate is partitioned into contributions from bulk and boundary layers, which is the essence of the Grossmann-Lohse (GL) theory on turbulent heat transfer.[15,16] We first calculate the locally averaged

thermal energy dissipation rates from the thermal boundary layer and the bulk as $\bar{\varepsilon}_{T,BL} = \left[\int_{0 \leq y \leq \delta_T} + \int_{H-\delta_T \leq y \leq H} \kappa(\partial_i T)^2 dy\right]/(2\delta_T) = \kappa\langle(\partial_i T(\mathbf{x} \in BL, t))^2\rangle_{V_{BL}}$ and $\bar{\varepsilon}_{T,bulk} = \left[\int_{\delta_T \leq y \leq H-\delta_T} \kappa(\partial_i T)^2 dy\right]/(H - 2\delta_T) = \kappa\langle(\partial_i T(\mathbf{x} \in bulk, t))^2\rangle_{V_{bulk}}$, respectively. Figure 7(a) shows the ratio of $\bar{\varepsilon}_{T,BL}$ and $\bar{\varepsilon}_{T,bulk}$ as a function of Rayleigh number. Here, the thermal boundary layer thickness δ_T is determined as the distance between the wall and the position at which the rms temperature is maximum. We can observe thermal energy dissipation rate that comes from the boundary layer region is an order of magnitude larger than that from the bulk region. With increasing
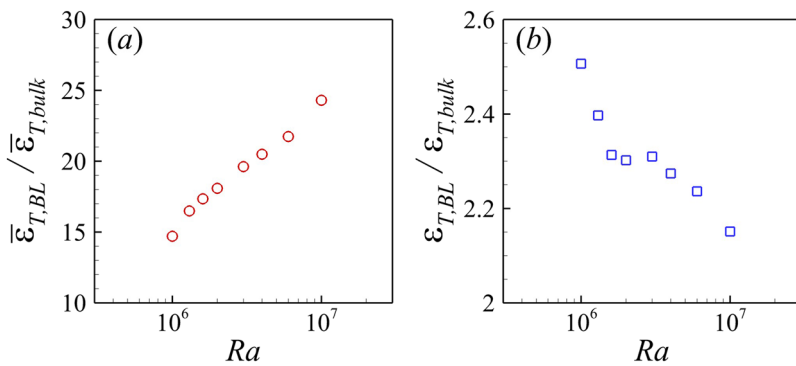

FIG. 7. Ratio of (a) locally averaged and (b) globally averaged thermal energy dissipation rates from the thermal boundary layer and the bulk.
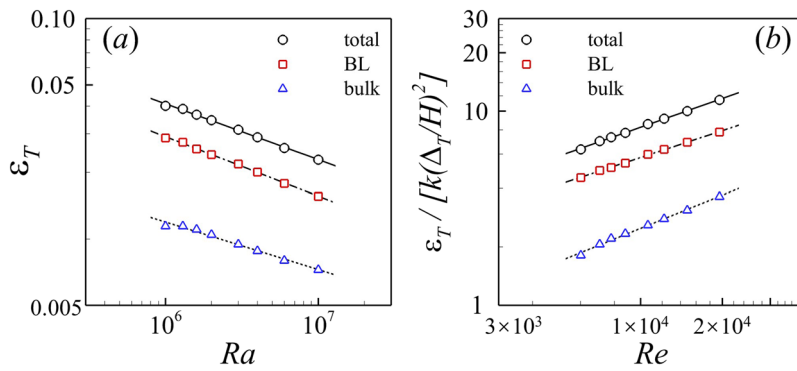
FIG. 8. (a) Thermal energy dissipation rates as a function of Ra; (b) normalized thermal energy dissipation rates as a function of Re. The lines are the power-law fits to the corresponding data.

Rayleigh number, thermal energy dissipation rate in the boundary layer is more intense. We further calculate the globally averaged thermal energy dissipation rates from the thermal boundary layer and the bulk as $\varepsilon_{T,BL} = \left[\int_{0 \leq y \leq \delta_T} + \int_{H-\delta_T \leq y \leq H} \kappa(\partial_i T)^2 dy\right]/H = \kappa\langle(\partial_i T(\mathbf{x} \in BL, t))^2\rangle_V$ and $\varepsilon_{T,bulk} = \left[\int_{\delta_T \leq y \leq H-\delta_T} \kappa(\partial_i T)^2 dy\right]/H = \kappa\langle(\partial_i T(\mathbf{x} \in bulk, t))^2\rangle_V$, respectively. Figure 7(b) shows the ratio of $\varepsilon_{T,BL}$ and $\varepsilon_{T,bulk}$ as a function of Rayleigh number. Although the boundary layer region occupies much smaller volume than the bulk region, we can still observe that more thermal energy is dissipated in the boundary layer region compared to that in the bulk region.

Globally averaged thermal energy dissipation rates a function of Rayleigh number are shown in Fig. 8(a). For the total thermal energy dissipation rate over the whole cell, the data can be well described by a power-law relation $\varepsilon_{T,total} = 1.35 Ra^{-0.25}$, indicated by the solid line in the figure. This scaling exponent is larger than that for $Pr = 0.7$ and $Pr = 0.53$ obtained from direct numerical simulations in a two-dimensional cell,[21] where the exponent is -0.20. On the other hand, the scaling behavior can be understood based on the global exact relation[14] of $\varepsilon_{T,total} = Nu/\sqrt{RaPr}$. Since we have obtained $Nu \sim Ra^{0.25}$ for $Pr = 0.025$ in Sec. III A, substituting the $Nu \sim Ra$ scaling into the global exact relation, we have $\varepsilon_{T,total} \sim Ra^{-0.25}$. The excellent agreement in the scaling exponent also demonstrates that the global exact relations are satisfied in our simulations. For the thermal energy dissipation rates from the boundary layer and bulk, the scaling behavior can be described by $\varepsilon_{T,BL} = 1.20 Ra^{-0.27}$ and $\varepsilon_{T,bulk} = 0.24 Ra^{-0.22}$, respectively. Figure 8(b) further shows the normalized globally averaged thermal dissipation rates $\varepsilon_T/[\kappa(\Delta_T/H)^2]$ as a function of Reynolds number. For the normalized total thermal energy dissipation rate over the whole cell, the data can be well described by a power-law relation $\varepsilon_{T,total}/[\kappa(\Delta_T/H)^2] \sim Re^{0.49}$. This scaling behavior can also be understood based on the global exact relation[14] of $\varepsilon_{T,total} = \kappa\Delta_T^2/H^2 Nu$ as follows: since we have obtained $Nu \sim Ra^{0.25}$ and $Re \sim Ra^{0.50}$ for $Pr = 0.025$ in Sec. III A, substituting the $Nu \sim Re^{0.50}$ relation into the global exact relation, we have $\varepsilon_{T,total}/[\kappa(\Delta_T/H)^2] \sim Re^{0.50}$. Again, the excellent agreement in the scaling exponent demonstrates that the global exact relations are satisfied in our simulations. As for the boundary layer and bulk regions, compared with moderate-Prandtl number convection in the same convection cell,[21] in the current low-Prandtl case, the scaling exponent of $\varepsilon_{T,BL}/[\kappa(\Delta_T/H)^2] \sim Re^{0.46}$ in the boundary layer region is slight smaller, while the scaling exponent

of $\varepsilon_{T,bulk}/[\kappa(\Delta_T/H)^2] \sim Re^{0.57}$ in the bulk region is significantly larger.

IV. CONCLUSIONS

In this work, we have presented high-resolution direct numerical simulations of a low-Prandtl number thermal convective flow and analyzed the statistical properties of temperature and thermal energy dissipation rate. The main findings are summarized as follows:

1. For a low Prandtl number of $Pr = 0.025$, the global heat transport and momentum scaling are $Nu = 0.21 Ra^{0.25}$ and $Re = 6.11 Ra^{0.50}$, respectively. Both the exponents of $Nu(Ra)$ and $Re(Ra)$ are smaller than those for a moderate Prandtl number in the same convection cell.
2. Locally averaged thermal energy dissipation rate from the boundary layer region is an order of magnitude larger than that from the bulk region. Even if the much smaller volume occupied by the boundary layer region is considered, the *globally averaged* thermal energy dissipation rate from the boundary layer region is still larger than that from the bulk region.
3. The scaling exponents of globally averaged thermal energy dissipation rates with Rayleigh and Reynolds numbers are numerically determined as $\varepsilon_{T,total} \sim Ra^{-0.25}$ and $\varepsilon_{T,total}/[\kappa(\Delta_T/H)^2] \sim Re^{0.49}$, and the scaling exponents are in excellent agreement with the global exact relation. Compared with moderate-Prandtl number convection in the same cell, in the current low-Prandtl case the scaling exponent of $\varepsilon_{T,bulk} \sim Re^{0.57}$ is significantly larger; while the scaling exponent of $\varepsilon_{T,BL} \sim Re^{0.46}$ is slightly smaller.

SUPPLEMENTARY MATERIAL

See the supplementary material for the video of instantaneous temperature and flow fields in both low- and moderate-Prandtl number turbulent thermal convection.

ACKNOWLEDGMENTS

and the 111 project of China (No. B17037). The simulations were carried out at LvLiang Cloud Computing Center of China, and the calculations were performed on TianHe-2.

APPENDIX: SIMULATION SETTINGS FOR MODERATE-PRANDTL NUMBER CONVECTION

We simulated turbulent thermal convection at a moderate Prandtl number (i.e., $Pr = 5.3$ and $Ra = 10^7$) to compare with low-Prandtl number convection. The mesh size was chosen as 257^2, which resulted in $\Delta_g/\eta \approx 0.18$, $\Delta_g/\eta_B \approx 0.41$, and $\Delta_t/\tau_\eta \approx 0.000\,34$ (see Sec. II C for the definition of Δ_g, η, η_B, Δ_t, and τ_η). A total run-time of 1000 free-fall time units were adopted to obtain statistically convergent results.

REFERENCES

[1] S. Hanasoge, L. Gizon, and K. R. Sreenivasan, "Seismic sounding of convection in the Sun," Annu. Rev. Fluid Mech. **48**, 191–217 (2016).

[2] E. M. King and J. M. Aurnou, "Turbulent convection in liquid metal with and without rotation," Proc. Natl. Acad. Sci. U. S. A. **110**, 6688–6693 (2013).

[3] G. Grötzbach, "Challenges in low-Prandtl number heat transfer simulation and modelling," Nucl. Eng. Des. **264**, 41–55 (2013).

[4] D. H. Kelley and D. R. Sadoway, "Mixing in a liquid metal electrode," Phys. Fluids **26**, 057102 (2014).

[5] G. Ahlers, S. Grossmann, and D. Lohse, "Heat transfer and large scale dynamics in turbulent Rayleigh-Bénard convection," Rev. Mod. Phys. **81**, 503 (2009).

[6] D. Lohse and K.-Q. Xia, "Small-scale properties of turbulent Rayleigh-Bénard convection," Annu. Rev. Fluid Mech. **42**, 335 (2010).

[7] F. Chillà and J. Schumacher, "New perspectives in turbulent Rayleigh-Bénard convection," Eur. Phys. J. E **35**, 58 (2012).

[8] K.-Q. Xia, "Current trends and future directions in turbulent thermal convection," Theor. Appl. Mech. Lett. **3**, 052001 (2013).

[9] A. Mazzino, "Two-dimensional turbulent convection," Phys. Fluids **29**, 111102 (2017).

[10] T. Vogt, S. Horn, A. M. Grannan, and J. M. Aurnou, "Jump rope vortex in liquid metal convection," Proc. Natl. Acad. Sci. U. S. A. **115**, 12674–12679 (2018).

[11] J. Schumacher, P. Götzfried, and J. D. Scheel, "Enhanced enstrophy generation for turbulent convection in low-Prandtl-number fluids," Proc. Natl. Acad. Sci. U. S. A. **112**, 9530–9535 (2015).

[12] J. D. Scheel and J. Schumacher, "Global and local statistics in turbulent convection at low Prandtl numbers," J. Fluid Mech. **802**, 147–173 (2016).

[13] L. Zwirner and O. Shishkina, "Confined inclined thermal convection in low-Prandtl-number fluids," J. Fluid Mech. **850**, 984–1008 (2018).

[14] B. I. Shraiman and E. D. Siggia, "Heat transport in high-Rayleigh-number convection," Phys. Rev. A **42**, 3650 (1990).

[15] S. Grossmann and D. Lohse, "Scaling in thermal convection: A unifying theory," J. Fluid Mech. **407**, 27–56 (2000).

[16] S. Grossmann and D. Lohse, "Prandtl and Rayleigh number dependence of the Reynolds number in turbulent thermal convection," Phys. Rev. E **66**, 016305 (2002).

[17] S. Grossmann and D. Lohse, "Fluctuations in turbulent Rayleigh–Bénard convection: The role of plumes," Phys. Fluids **16**, 4462–4472 (2004).

[18] M. Emran and J. Schumacher, "Fine-scale statistics of temperature and its derivatives in convective turbulence," J. Fluid Mech. **611**, 13–34 (2008).

[19] M. Overholt and S. Pope, "Direct numerical simulation of a passive scalar with imposed mean gradient in isotropic turbulence," Phys. Fluids **8**, 3128–3148 (1996).

[20] M. Kaczorowski and C. Wagner, "Analysis of the thermal plumes in turbulent Rayleigh–Bénard convection based on well-resolved numerical simulations," J. Fluid Mech. **618**, 89–112 (2009).

[21] Y. Zhang, Q. Zhou, and C. Sun, "Statistics of kinetic and thermal energy dissipation rates in two-dimensional turbulent Rayleigh–Bénard convection," J. Fluid Mech. **814**, 165–184 (2017).

[22] Y. Zhang, Y.-X. Huang, N. Jiang, Y.-L. Liu, Z.-M. Lu, X. Qiu, and Q. Zhou, "Statistics of velocity and temperature fluctuations in two-dimensional Rayleigh-Bénard convection," Phys. Rev. E **96**, 023105 (2017).

[23] S. Bhattacharya, A. Pandey, A. Kumar, and M. K. Verma, "Complexity of viscous dissipation in turbulent thermal convection," Phys. Fluids **30**, 031702 (2018).

[24] S. Chen and G. D. Doolen, "Lattice Boltzmann method for fluid flows," Annu. Rev. Fluid Mech. **30**, 329–364 (1998).

[25] C. K. Aidun and J. R. Clausen, "Lattice-Boltzmann method for complex flows," Annu. Rev. Fluid Mech. **42**, 439–472 (2010).

[26] A. Xu, W. Shyy, and T. Zhao, "Lattice Boltzmann modeling of transport phenomena in fuel cells and flow batteries," Acta Mech. Sin. **33**, 555–574 (2017).

[27] H. Yu, S. S. Girimaji, and L.-S. Luo, "DNS and LES of decaying isotropic turbulence with and without frame rotation using lattice Boltzmann method," J. Comput. Phys. **209**, 599–616 (2005).

[28] P. Wang, L.-P. Wang, and Z. Guo, "Comparison of the lattice Boltzmann equation and discrete unified gas-kinetic scheme methods for direct numerical simulation of decaying turbulent flows," Phys. Rev. E **94**, 043304 (2016).

[29] C. Peng, N. Geneva, Z. Guo, and L.-P. Wang, "Direct numerical simulation of turbulent pipe flow using the lattice Boltzmann method," J. Comput. Phys. **357**, 16–42 (2018).

[30] C. Peng, O. M. Ayala, and L.-P. Wang, "A direct numerical investigation of two-way interactions in a particle-laden turbulent channel flow," J. Fluid Mech. **875**, 1096–1144 (2019).

[31] A. Xu, L. Shi, and H.-D. Xi, "Lattice Boltzmann simulations of three-dimensional thermal convective flows at high Rayleigh number," Int. J. Heat Mass Transfer **140**, 359–370 (2019).

[32] Z. Guo, C. Zheng, and B. Shi, "Discrete lattice effects on the forcing term in the lattice Boltzmann method," Phys. Rev. E **65**, 046308 (2002).

[33] F. Dubois and P. Lallemand, "Towards higher order lattice Boltzmann schemes," J. Stat. Mech.: Theory Exp. **2009**, P06006.

[34] J. Wang, D. Wang, P. Lallemand, and L.-S. Luo, "Lattice Boltzmann simulations of thermal convective flows in two dimensions," Comput. Math. Appl. **65**, 262–286 (2013).

[35] D. Contrino, P. Lallemand, P. Asinari, and L.-S. Luo, "Lattice-Boltzmann simulations of the thermally driven 2D square cavity at high Rayleigh numbers," J. Comput. Phys. **275**, 257–272 (2014).

[36] A. Xu, L. Shi, and T. Zhao, "Accelerated lattice Boltzmann simulation using GPU and OpenACC with data management," Int. J. Heat Mass Transfer **109**, 577–588 (2017).

[37] R. M. Kerr, "Rayleigh number scaling in numerical convection," J. Fluid Mech. **310**, 139–179 (1996).

[38] O. Shishkina and C. Wagner, "Local heat fluxes in turbulent Rayleigh-Bénard convection," Phys. Fluids **19**, 085107 (2007).

[39] W.-F. Zhou and J. Chen, "Letter: Similarity model for corner roll in turbulent Rayleigh-Bénard convection," Phys. Fluids **30**, 111705 (2018).

[40] S. Cioni, S. Ciliberto, and J. Sommeria, "Strongly turbulent Rayleigh–Bénard convection in mercury: Comparison with results at moderate Prandtl number," J. Fluid Mech. **335**, 111–140 (1997).

[41] J. D. Scheel and J. Schumacher, "Predicting transition ranges to fully turbulent viscous boundary layers in low Prandtl number convection flows," Phys. Rev. Fluids **2**, 123501 (2017).

[42] E. P. van der Poel, R. J. Stevens, and D. Lohse, "Comparison between two- and three-dimensional Rayleigh–Bénard convection," J. Fluid Mech. **736**, 177–194 (2013).

[43] Y.-Z. Zhang, C. Sun, Y. Bao, and Q. Zhou, "How surface roughness reduces heat transport for small roughness heights in turbulent Rayleigh–Bénard convection," J. Fluid Mech. **836**, R2 (2018).

[44] H. Johnston and C. R. Doering, "Comparison of turbulent thermal convection between conditions of constant temperature and constant flux," Phys. Rev. Lett. **102**, 064501 (2009).

[45] E. P. van der Poel, R. J. Stevens, K. Sugiyama, and D. Lohse, "Flow states in two-dimensional Rayleigh-Bénard convection as a function of aspect-ratio and Rayleigh number," Phys. Fluids **24**, 085104 (2012).

[46] K. Sugiyama, E. Calzavarini, S. Grossmann, and D. Lohse, "Flow organization in two-dimensional non-Oberbeck–Boussinesq Rayleigh–Bénard convection in water," J. Fluid Mech. **637**, 105–135 (2009).

[47] Y.-X. Huang and Q. Zhou, "Counter-gradient heat transport in two-dimensional turbulent Rayleigh–Bénard convection," J. Fluid Mech. **737**, 1–12 (2013).

[48] F. Heslot, B. Castaing, and A. Libchaber, "Transitions to turbulence in helium gas," Phys. Rev. A **36**, 5870 (1987).

[49] B. Castaing, G. Gunaratne, F. Heslot, L. Kadanoff, A. Libchaber, S. Thomae, X.-Z. Wu, S. Zaleski, and G. Zanetti, "Scaling of hard thermal turbulence in Rayleigh-Bénard convection," J. Fluid Mech. **204**, 1–30 (1989).

[50] H.-D. Xi, S. Lam, and K.-Q. Xia, "From laminar plumes to organized flows: The onset of large-scale circulation in turbulent thermal convection," J. Fluid Mech. **503**, 47–56 (2004).

[51] A. N. Kolmogorov, "A refinement of previous hypotheses concerning the local structure of turbulence in a viscous incompressible fluid at high Reynolds number," J. Fluid Mech. **13**, 82–85 (1962).

[52] Q. Zhou and L.-F. Jiang, "Kinetic and thermal energy dissipation rates in two-dimensional Rayleigh-Taylor turbulence," Phys. Fluids **28**, 045109 (2016).